

Unravelling the Role of Metal-Metal Oxide Interfaces of Cu/ZnO/ZrO₂/Al₂O₃ Catalyst for Methanol Synthesis from CO₂: Insights from Experiments and DFT-based Microkinetic Modeling

Balaji C Dharmalingam^{a,#}, Ajay Koushik V^{a,#}, Mauro Mureddu^b, Luciano Atzori^{b,c}, Sarah Lai^b, Alberto Pettinau^b, Niket S Kaisare^{a,*}, Preeti Aghalayam^{a,*}, Jithin John Varghese^{a,*}

^a Department of Chemical Engineering, Indian Institute of Technology Madras, Chennai 600036, India

^b Sotacarbo S.p.A., Grande Miniera di Serbariu, Carbonia 09013, Italy

^c Department of Chemical and Geological Sciences, University of Cagliari, 09042 Monserrato, Italy

*Corresponding authors' email: nkaisare@iitm.ac.in, preeti@iitm.ac.in, jithinjv@iitm.ac.in

These authors contributed equally to this work and should be considered co-first authors

Abstract

Cu/ZnO/ZrO₂/Al₂O₃ catalysts are widely explored for CO₂ conversion to methanol due to their higher activity and stability. However, mechanistic understanding of the performance of such catalysts is lacking due to ambiguity on the actual active sites. This study focuses on unraveling the nature of different interfaces on Cu/ZnO/ZrO₂/Al₂O₃ catalyst by coupling experiments, Density Functional Theory (DFT) simulations and a DFT-based reactor scale multi-site microkinetic model. Although DFT calculations suggested the Zr/Cu interface to be the CO₂ adsorption site, the validated microkinetic model predicted the Zn/Cu interface to be the crucial reaction center. Reaction pathway analysis showed that methanol is produced through the formate pathway near the reactor entrance, whereas, the carboxyl pathway dominates in the latter zones, emphasizing the occurrence of both CO₂ and CO hydrogenation. This deeper understanding of the reaction behavior of such multicomponent catalysts will aid in designing better catalysts and optimizing reaction conditions and systems.

Keywords: DFT, Microkinetic modeling, Methanol production, CO₂ hydrogenation, Copper-Zinc-Zirconia, Multiscale modeling,

1 Introduction

Carbon dioxide is one of the important greenhouse gases released into the earth's atmosphere, raising global temperature, which is increasing at an average rate of 0.18 °C per decade since 1981 [1]. There is a need to cut down the anthropogenic CO₂ emission and sequester or utilize CO₂ to limit the temperature rise to 1.5 °C above the pre-industrial levels [2]. Carbon Capture Utilization and Storage (CCUS) is proven to mitigate the impact of CO₂ emissions [3,4]. Among the available routes for CO₂ mitigation, utilizing CO₂ has gained attention, as CO₂ can act as a potential feedstock for producing value-added chemicals [4]. One such way of the utilization of CO₂ as a feedstock is thermocatalytic reduction using H₂ from sources such as solar, wind, or other renewables to produce methanol, methane, syngas, and other organic compounds [5,6]. Methanol

1
2
3
4 production from CO₂ hydrogenation has gained importance because it is cleaner compared to the
5 other fuels and is a potential hydrogen carrier. It can also be used as a feedstock to produce other
6 commodity chemicals such as acetic acid, dimethyl ether, and higher hydrocarbons.
7
8

9
10 Catalysts play a critical role in lowering the energy requirements for the reduction reaction and in
11 the selective production of methanol. Typical industrial production of methanol is carried out from
12 CO-rich syngas at a temperature of 200-300 °C and high pressure of 50-100 bar in the presence of
13 Cu/ZnO/Al₂O₃ catalysts [7]. However, this catalyst is unstable for CO₂-rich feeds due to water
14 formation from CO₂ hydrogenation [8]. Addition of promoters such as ZrO₂ [9], CeO₂ [10,11] or
15 both [12,13] to the Cu/ZnO/Al₂O₃ catalyst to improve its performance for CO₂-rich feeds were
16 explored. Numerous investigations have demonstrated the superior performance of the ternary
17 Cu/ZnO/ZrO₂ [14–22] catalyst towards enhanced methanol yield during CO₂ hydrogenation. The
18 presence of Zr in the Cu/ZnO/Al₂O₃ catalysts help inhibit water poisoning due to its weak
19 hydrophilic character, thereby increasing its stability and sustained performance [19]. Owing to its
20 basic nature, Zr also is known to enhance CO₂ sorption capacity of the catalyst [21,23] and this
21 surface basicity is believed to improve methanol selectivity [21]. This indicates a direct
22 participation of Zr or an appropriate interface involving Zr[24,25] in the multicomponent catalyst,
23 in the reaction mechanism, thereby directing the selective formation of methanol. Some other
24 investigations however point to an indirect role of Zr in catalytic performance. Its presence was
25 shown to enrich the physicochemical properties of the catalyst such as Cu dispersion (D_{Cu}) and Cu
26 surface area (S_{Cu}) which also enhance CO₂ conversion [26,27]. Despite much experimental and
27 computational efforts, the synergy between the multiple catalyst components that enhances
28 methanol yield remains unclear. On this note, it is critical to explore the role of individual
29 components in the ternary catalyst to design superior materials.
30
31
32
33
34
35
36
37
38

39 Density Functional Theory (DFT) calculations are handy in understanding detailed catalytic
40 reaction mechanisms, and exploring the role of interfacial interaction of binary catalysts (Cu/ZnO
41 [28,29], Cu/ZrO₂ [25,30,31] and ZnO/ZrO₂ [32]). A few studies on the binary catalysts emphasize
42 the importance of metal-metal/metal oxide interface for CO₂ adsorption [33,34]. However, limited
43 studies focus on explaining the mechanistic roles of the different components that lead to enhanced
44 performance of the ternary Cu/ZnO/ZrO₂ catalysts. Wang et al. [35] studied the interaction of
45 different components in the ternary Cu/ZnO/ZrO₂ (CZZ) catalyst using in situ Diffuse Reflectance
46 Infrared Fourier Transform Spectroscopy (DRIFTS) and DFT calculations. Although several
47 reaction pathways involving intermediates such as the formate (HCOO), carboxyl (COOH) and
48 CO (directly from CO₂ dissociation) are proposed in the literature [24], the DFT study of the
49 reaction mechanism by Wang et al. [35] was restricted only to the formate pathway on the ZnO-
50 ZrO₂ catalyst model based on their in-situ DRIFTS data which confirmed its presence on the
51 catalyst surface. Based on the DFT and DRIFTS analyses, they proposed the reaction to proceed
52 on the ZnO-ZrO₂ interface with hydrogen activated on the copper surface. In typical computational
53 investigations of catalysts with multiple active sites or interfaces, the site with the strongest
54
55
56
57
58
59
60
61
62
63
64
65

1
2
3
4 reactant binding energy is usually considered as the favorable site for reaction, and all further
5 mechanistic analyses are done on that site [23,33,36]. Moreover, if one of the potential parallel
6 pathways for methanol formation has a comparatively higher activation barrier, it is typical to
7 neglect that particular pathway (typically the carboxyl pathway in this case) for further analyses
8 [36,37]. Moreover, to the best of the authors' knowledge, there is no validated detailed kinetic
9 model available for the ternary catalyst that will enable prediction of reaction behavior and
10 optimization of operating conditions for the best yield of methanol.
11
12
13
14

15 Hence, this paper presents a comprehensive analysis of the methanol synthesis reaction on the
16 Cu/ZnO/ZrO₂ ternary catalyst using a combination of reactor experiments, detailed DFT
17 simulations and multi-site reactor-scale microkinetic modeling. For the mechanistic analysis using
18 DFT simulations, a catalyst model with all three components and three active sites: the Zn/Cu
19 interface, the Zr/Cu interface and Cu was considered. All possible reactions happening on both
20 these sites were analyzed simultaneously to unravel the role of all three sites and all the pathways
21 in methanol formation. Inputs from these were used to build a detailed multi-site microkinetic
22 model which considered all three sites and a reaction network comprising all pathways on both the
23 interfaces simultaneously which was validated against our reactor performance data, via reactor
24 scale simulations. It is showed that this approach and the reactor scale DFT-microkinetic analyses
25 gave different insights on the operando reaction mechanisms and the reaction progress along the
26 packed bed reactor, compared to what was possible with the approximations mentioned earlier,
27 which led to incomplete or misleading interpretations.
28
29
30
31
32
33
34

35 The manuscript is organized as follows. Section 2 presents the methodologies adopted in catalyst
36 synthesis, characterization, and catalytic activity tests in the packed bed reactor, followed by the
37 computational methods adopted in DFT modeling of the reaction network on the model ternary
38 catalyst and the details of the multisite microkinetic modeling framework. Section 3 starts with a
39 brief description of the catalyst characterization and is followed by the justification and rationale
40 for the computational catalyst model adopted for the detailed DFT simulations. Next, the details
41 pertaining to the DFT analyses of all the reaction pathways and associated energetics on different
42 active sites are presented. This is followed by the development and validation of the detailed multi-
43 site reactor scale microkinetic model that predicts our experimental observables such as conversion
44 and product flow rates. Further, the reaction pathway analysis (RPA) is presented, where unique
45 insights on the sites for reaction progress, pertinent mechanisms and how the reaction progressed
46 along the reactor bed were obtained. This approach and analysis gave a deeper understanding of
47 the reaction behavior that could be used for the rational design of catalysts for conducting the
48 reaction under milder conditions.
49
50
51
52
53
54
55
56
57
58
59
60
61
62
63
64
65

2 Methodology

2.1 Catalyst synthesis procedure

The synthesis method and physicochemical characterization of the $\text{Cu}_2\text{Zn}_1\text{Al}_{0.7}\text{Zr}_{0.3}$ catalyst are reported in detail in our previous work [38], and it is briefly summarized here. An aqueous solution (100 cm^3 , with total concentration of 1.5 M) containing appropriate amounts of $\text{Cu}(\text{NO}_3)_2$, $\text{Al}(\text{NO}_3)_3$, $\text{Zn}(\text{NO}_3)_2$ and $\text{ZrO}(\text{NO}_3)_2$ was first prepared. A second solution containing 7.15 g of Na_2CO_3 and 13.95 g of NaOH in 100 cm^3 of distilled water was then added slowly using a peristaltic pump to the former solution at room temperature under stirring to maintain the pH constant at 11. The solution was kept at 60°C for 20 h and the resulting hydrotalcite was dried at 80°C overnight and finally calcined at 500°C for 4 h to obtain the catalyst.

2.2 Catalyst characterization

The chemical composition of the synthesized catalyst was determined by inductively coupled plasma atomic emission spectroscopy (ICP-AES) with a Liberty 200 spectrophotometer (Varian, Palo Alto, California, CA, USA). Samples (*ca.* 0.015 g) were dissolved in 2 cm^3 of a mixture of HCl (37%) and HNO_3 (70%) (3:1 by volume). After 24 h, the solutions were diluted to 250 cm^3 with Milli-Q water and analyzed.

The X-ray diffraction (XRD) analysis was performed on the fresh and the H_2 -treated (5 vol% H_2 in N_2 ; flow rate, 15 $\text{cm}^3 \text{min}^{-1}$ at 250 °C for 2 h) samples. XRD patterns were recorded on a X'pert Pro diffractometer (Panalytical, Malvern, UK) with θ - θ Bragg-Brentano geometry, $\text{Cu-K}\alpha 1$ wavelength radiation ($\lambda = 1.5418 \text{ \AA}$) and X'Celerator detector, operating at 40 kV and 40 mA. The crystallite size was estimated by the Scherrer equation using the Warren correction [39].

Adsorption microcalorimetry measurements were performed with a Tian–Calvet heat flow calorimeter (Setaram, Caluire, France) equipped with a volumetric vacuum line. Each sample (*ca.* 0.1 g, 40–80 mesh), as prepared or previously H_2 -treated (5 vol% H_2 in N_2 ; flow rate, 15 $\text{cm}^3 \text{min}^{-1}$ at 250 °C for 2 h), was thermally pretreated at 220 °C for 12 h under vacuum (5×10^{-3} Pa). Adsorption was carried out by admitting successive doses of CO_2 as the probe gas at 80 °C to limit physisorption. The equilibrium pressure relative to each adsorbed amount was measured utilizing a differential pressure gauge, and the thermal effect was recorded. The run was stopped at a final equilibrium pressure of 133 Pa.

Temperature-programmed reduction (TPR) profiles were recorded with 0.030 g of catalyst on a TPD/R/O 1100 apparatus (Thermo Fisher Scientific, Waltham, Massachusetts, MA, USA) from 50 to 400 °C, at 10 °C min^{-1} , under 30 $\text{cm}^3 \text{min}^{-1}$ flow of 5 vol% H_2 in N_2 . Before the experiment, samples were pretreated in nitrogen (20 $\text{cm}^3 \text{min}^{-1}$) at 350 °C for 2 h. The hydrogen consumption was monitored by a thermal conductivity (TCD) detector.

2.3 Catalytic activity

The performance evaluation for CO₂ hydrogenation to methanol was conducted in a customized Microactivity Efficient, PID Eng&Tech bench-scale plant, employing a high-pressure fixed bed stainless steel reactor (9.1 mm I.D. x 304.8 mm long) [40,41]. A porous plate (made of Hastelloy C, 20 μm in size) and quartz wool were used to support the catalytic bed inside the isothermal temperature zone of the reactor. 1.0 g of calcined catalyst was diluted with α-Al₂O₃ and loaded into the reactor to obtain a total bed volume of ca. 3 cm³. The catalyst was in-situ reduced in a stream of 15% v/v H₂/N₂ at 250 °C for 2 h under atmospheric pressure and 270 sccm flow. Upon completion of the reduction process, the reactant mixture was sent to the reactor, and the temperature varied between 200 °C and 250 °C. The catalyst activity was measured at pressures ranging from 3.0 to 7.0 MPa. Each run was held for 10 h in the same operating condition to reach a stationary catalytic behavior. The reaction stream was analyzed by a gas chromatograph (Agilent 7890B, Santa Clara, California, CA, USA) equipped with flame ionized detector (FID, for carbon-containing compounds) and thermal conductivity detector (TCD, for permanent gases), and two columns HP-Plot Q column (30m × 0.53mm × 40 μm) used to separate and identify CO₂, methanol, dimethyl ether, C₂ and C₃ hydrocarbons and a HP-Plot Molesieve 5A (30m × 0.53mm × 50 μm) for H₂, N₂, CH₄ and CO. To avoid condensation of condensable products, connections between the plant gas outlet and GC inlet were heated at 180°C. Nitrogen was used as an internal standard. CO₂ conversion (X_{CO₂}) and products selectivity (S_{CO}, S_{CH₃OH}, and S_{DME}), were calculated as follows:

$$X_{\text{CO}_2} = \frac{\left(\frac{\text{CO}_2}{\text{N}_2}\right)_{\text{in}} - \left(\frac{\text{CO}_2}{\text{N}_2}\right)_{\text{out}}}{\left(\frac{\text{CO}_2}{\text{N}_2}\right)_{\text{in}}} \times 100 \quad (1)$$

$$S_{\text{CH}_3\text{OH}} = \frac{\left(\frac{\text{CH}_3\text{OH}}{\text{N}_2}\right)_{\text{out}}}{\left(\frac{\text{CO}_2}{\text{N}_2}\right)_{\text{in}} - \left(\frac{\text{CO}_2}{\text{N}_2}\right)_{\text{out}}} \times 100 \quad (2)$$

$$S_{\text{CO}} = \frac{\left(\frac{\text{CO}}{\text{N}_2}\right)_{\text{out}}}{\left(\frac{\text{CO}_2}{\text{N}_2}\right)_{\text{in}} - \left(\frac{\text{CO}_2}{\text{N}_2}\right)_{\text{out}}} \times 100 \quad (3)$$

A wide range of operating conditions was covered to investigate the catalytic performance: The H₂/CO₂ molar ratio was varied between 3 and 6 mol mol⁻¹; pressures between 3.0 and 7.0 MPa; and Gas Hourly Space Velocity (GHSV) ranges between 4,500 and 13,000 h⁻¹. The GHSV was calculated as follows:

$$\text{GHSV (h}^{-1}\text{)} = \frac{\text{Inlet gas volume (cm}^3\text{/min)}}{\text{Catalytic Bed Volume (cm}^3\text{)}} \cdot 60 \text{ (min/h)} \quad (4)$$

All the catalytic studies were performed three times for each catalyst, and the values of the relative standard deviations obtained for the conversion and selectivity were in the range of 2–5%.

2.4 DFT methods

The DFT calculations were carried out using Vienna *Ab-initio* Simulation Package (VASP) code, version 5.4.4 [42]. The generalized gradient approximation of Perdew-Burke-Ernzerhof (PBE) [43] was employed for capturing the electronic exchange and correlation interactions. The plane wave pseudopotential implementation of DFT with kinetic energy expansion cut off 400 eV (1 eV (electron volt) = 96.4 kJ/mol), and the Projector Augmented Wave (PAW) [44] method for treatment of the core-valence electron interactions were used for all optimizations. The dispersion interactions which were not intrinsically accounted for in DFT, were incorporated using Grimme's DFT-D₃ method [45].

Bulk optimization of the copper unit cell was done, and the optimized lattice constant was found to be 3.586 Å which is in close agreement with the experimental value of 3.615 Å (1 Å = 0.1 nm) [46]. Cu (111) surface was modeled with a $p4 \times 5$ supercell with three atomic layers consisting of 60 Cu atoms. A vacuum region of 12 Å thickness was applied to avoid interaction between the slab and its periodic images in the z direction. The bottom layer of the Cu slab was fixed during the geometry optimization to represent the bulk Cu, while the rest of the atoms were allowed to relax. The metal-metal oxide catalyst was modeled by depositing a $Zr_1Zn_2O_3$ cluster on the Cu(111) surface, representing an inverse catalyst model of metal oxide on metal. The details of this catalyst model and justification for this choice are discussed in section 3.2. The Brillouin-zone for the $p4 \times 5$ supercell was sampled using $4 \times 4 \times 1$ Monkhorst-Pack [47] k-point distribution. The minimum energy paths and the respective transition states for each of the elementary steps were estimated using the Nudged Elastic Band (NEB) method and were further refined using the Improved Dimer Method (IDM) [48] implemented in VASP. The following equations were then used to calculate the adsorption energies and the activation energy barriers of the corresponding elementary steps.

The adsorption energy of a species was calculated using the formula:

$$E_{ads} = E_{slab+species} - E_{slab} - E_{gas\ species} \quad (5)$$

Where E_{ads} is the adsorption energy of the species in eV, $E_{slab+species}$ is the energy of the system where species is adsorbed on the catalyst slab in eV, E_{slab} is the energy of the pure catalyst slab in eV and $E_{gas\ species}$ is the energy of the species in the gas phase in eV.

The activation energy barrier was calculated as:

$$E_a = E_{TS} - E_r \quad (6)$$

Where E_a is the activation energy barrier of the elementary reaction steps in eV, E_{TS} is the energy of the transition state complex in eV and E_r is the energy of the reactant intermediate in eV.

Geometries of all reaction intermediates and transition states were confirmed to be minima and saddle points, respectively, using vibrational frequency analysis along the reaction coordinate. The

DFT calculated electronic energies were then corrected using the Zero Point Vibrational Energies (ZPVE). The free energies of the adsorption/desorption steps and elementary surface reactions were then obtained after incorporating the entropic contributions using statistical mechanics. The methodology for ZPVE and entropic corrections to the DFT potential energy are described in the supplementary material section S.1.

2.5 Microkinetic Model

A thermodynamically consistent microkinetic model was developed using data from the DFT simulations and was used to predict the bench-scale packed-bed reactor data. The reactor simulations were carried out using the Ansys CHEMKIN-PRO (2020 R1) software package [49] and an ideal steady-state isothermal plug flow reactor (PFR) model was used:

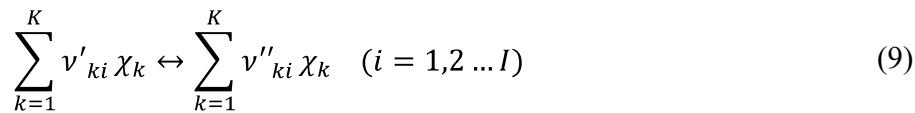
$$\frac{d(\rho u \omega_k)}{dz} = a_v W_k \sum_{i=1}^l v_{ki} r_i \quad k \in [1, n_{gas}] \quad (7)$$

Where ρ , u , ω_k and W_k are the density, the axial velocity, mass fraction of species k and the molecular weight (of species k) of the gas respectively. v_{ki} represents the stoichiometric coefficients of species k in reaction i . r_i represents the rate of the reaction i . a_v represents the area per unit volume of the catalyst.

For surface adsorbed species,

$$\Gamma \frac{d\theta_k}{dt} = 0 = \sum_{i=1}^l v_{ki} r_i \quad k \in [K_{Surface}] \quad (8)$$

Where Γ is the site density of the catalyst and θ_k is the fractional site coverage of species k . All the reactions in the microkinetic model are elementary reactions, represented as



Where v_{ki}' and v_{ki}'' are positive integers representing stoichiometric coefficients of reactants and products, respectively; $v_{ki} = v_{ki}' - v_{ki}''$ is the overall stoichiometric coefficient of reaction i ; and

$$r_i = k_{fi} \prod_{k=1}^K C_k^{v'_{ki}} - k_{ri} \prod_{k=1}^K C_k^{v''_{ki}} \quad (10)$$

is the rate of elementary reactions. These reaction rate constants were calculated using the Extended Arrhenius rate expression as follows

$$k_f = A_i T^\beta \exp\left(\frac{-E_i}{RT}\right) \quad (11)$$

A_i is the pre-exponential/frequency factor, β_i is the temperature exponent, E_i is the activation energy of the i^{th} reaction.

Figure 1 shows the schematic of the reaction mechanism considered in this work. The final thermodynamically consistent reaction mechanism with optimized parameters is summarized in Table S4 of supplementary material. Three different sites were considered: Cu sites where non-carbonaceous species (H#, OH#, H₂O#) can adsorb, and zinc-copper (Zn) and zirconium-copper (Zr) interfaces where rest of the species can adsorb. The formate (HCOO*) and carboxyl (COOH*) pathways on both Zn/Cu and Zr/Cu interfaces were explored. In the formate pathway, hydrogen is attached to the carbon of CO₂, whereas in the carboxyl pathway, hydrogen is attached to the free oxygen of adsorbed CO₂. Methanol, CO, formic acid, and water were considered as stable gas-phase products.

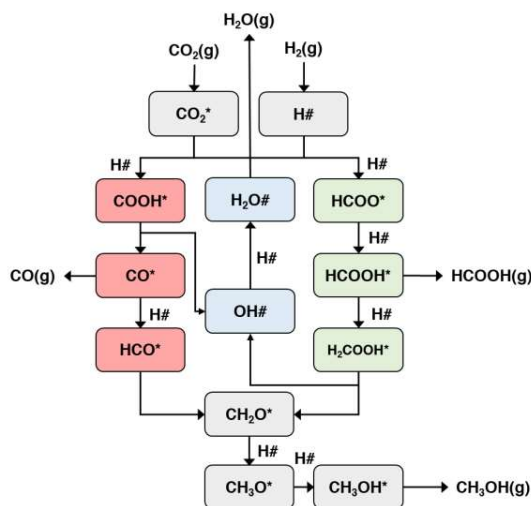


Figure 1-The schematic of the reaction network of CO₂ hydrogenation to methanol on the Cu/ZnO/ZrO₂ catalyst. The same set of reactions were considered to take place on both Zr/Cu and Zn/Cu interfaces. "*" (represents Zr/Cu and Zn/Cu sites) and "#" (represents pure Cu sites) indicate that the species is adsorbed on the surface. Colour codes: Green- Formate Pathway; Red- Carboxyl Pathway; Grey- Common Pathway; Blue- Water formation Pathway

The activation energy and the pre-exponential factor for the individual reactions were calculated using DFT simulations and transition state theory (TST) with appropriate statistical thermodynamics expressions (details of the estimation of the pre-exponential factors are provided in section S.1 of SI). The densities of different types of active sites were calculated based on our computational catalyst model. With 14 copper atoms available on the surface of the model catalyst supercell with an area of 128.6 Å², the site density of copper was $\Gamma_{\text{Cu}} = 1.81 \times 10^{-9}$ mol/cm². Similarly, Γ_{Zn} and Γ_{Zr} were 2.58×10^{-10} mol/cm² and 1.29×10^{-10} mol/cm², respectively.

In the literature, microkinetic models are sometimes built using kinetic parameters estimated for each reaction set and in some other cases, the preliminary model is refined by optimizing the kinetic parameters of a large number of reaction sets for better prediction of experimental data

[50–53]. Here, the preliminary kinetic model was built using the DFT derived kinetic parameters. Minimal optimization of the kinetic parameters of three forward/backward reaction sets for better prediction of our lab-scale experimental data was done and a validated kinetic model was thus obtained.

3 Results and Discussions

3.1 Catalyst characterization

The composition of the prepared catalyst samples was analyzed using the ICP-AES technique. The experimental composition of the synthesized Cu/Zn/Zr/Al catalyst was $\text{Cu}_2\text{Zn}_{1.02}\text{Al}_{0.81}\text{Zr}_{0.25}$ and was found to be in good match against the theoretical value ($\text{Cu}_2\text{Zn}_1\text{Al}_{0.7}\text{Zr}_{0.3}$).

The XRD patterns of the fresh and the reduced catalyst samples are shown in Figure 2. XRD of the fresh catalyst showed the typical signal associated with the CuO phase, for which a mean crystallite size of 11 nm was estimated. In addition, peaks with very low intensity associated with the presence of the ZnO phase (PDF Card 75-0576) were observed, even though not clearly defined due to the superimposition with the more evident one of CuO. No peaks associated with Al_2O_3 phases were visible, probably due to its predominant amorphous character; the absence of peaks ascribable to the ZrO_2 phase can be justified accordingly. The reduced sample exhibited clear wide peaks at $2\theta = ca. 43.3^\circ$ and 50.6° indicating the presence of face centred cubic metallic copper (Cu^0 with space group $Fm\bar{3}m$) together with the presence of relatively low intensity diffraction peaks at $2\theta = ca. 32.4^\circ$, 36.4° and 56.9° attributed to the most intense reflection of the hexagonal zinc oxide phase (ZnO with space group $P63mc$). The TPR profiles (Figure S1) indicated the reduction of CuO in the catalyst and the reduction of CuO to Cu is evident in the XRD pattern of the reduced catalyst.

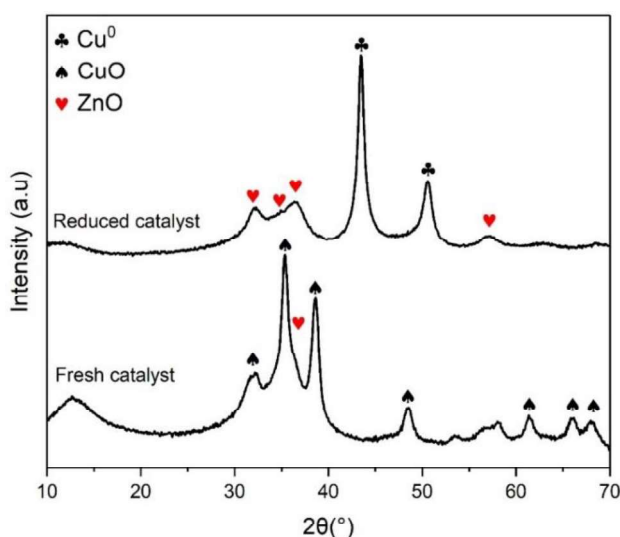


Figure 2-XRD pattern of the fresh and the reduced $\text{Cu}_2\text{Zn}_1\text{Al}_{0.7}\text{Zr}_{0.3}$ catalyst. The reduced sample was H_2 -treated (5 vol% H_2 in N_2 ; flow rate, $15 \text{ cm}^3 \text{ min}^{-1}$ at 250°C for 2 h)

3.2 Development and validation of the computational catalyst model

The computational catalyst model was developed based on the aforementioned information from the characterization of the $\text{Cu}_2\text{Zn}_1\text{Al}_{0.7}\text{Zr}_{0.3}$ catalyst. As TPR analysis (Figure S1) and XRD pattern of the reduced catalyst (Figure 2) indicated the reduction of CuO to Cu, the catalyst was modeled to contain metallic copper. XRD pattern of the reduced catalyst indicated the presence of poorly crystalline ZnO and finely dispersed ZrO_2 (no distinct peaks observed). Gao et al. [21] reported the existence of strong interactions between CuO, ZnO and ZrO_2 in $\text{Cu}/\text{ZnO}/\text{ZrO}_2/\text{Al}_2\text{O}_3$ catalyst prepared by a hydrotalcite method, similar to the approach adopted in this work. This was based on the absence of distinct ZnO and ZrO_2 peaks in the XRD patterns and the analyses of the X-Ray Photoelectron Spectra (XPS) of the catalyst. A similar behavior in our XRD pattern was observed and hence, direct interaction of ZnO and ZrO_2 in the catalyst was expected. Based on these inferences, the catalyst was modeled as an inverse catalyst with $\text{ZrO}_x/\text{ZnO}_x$ deposited on metallic Cu surface. The (111) surface of Cu was chosen to represent the metallic state of Cu and a Zn_xO_y motif ($x=3$ and $y=1$) denoted as Zn_3O was chosen, which was found to be an approximate form of bulk wurtzite ZnO structure [54,55]. In this, a Zr atom was incorporated by substitutional replacement of one of the Zn atoms of the Zn_3O motif and two oxygen atoms were added to represent the $\text{ZrO}_x/\text{ZnO}_x/\text{Cu}$ inverse catalyst. Hereafter the catalyst model is denoted as $\text{Zr}_1\text{Zn}_2\text{O}_3/\text{Cu}(111)$ and a schematic representation of the same catalyst model is shown in Figure S2.

The validity of the features of the proposed computational catalyst model was ascertained by 1) comparison of DFT based CO_2 adsorption studies on the model catalyst against microcalorimetric measurements of CO_2 adsorption on the reduced catalyst, and 2) comparison of the computational IR spectra of key intermediates in CO_2 reduction on the catalyst model (details in section S.4 of SI) with operando DRIFTS data of the same species on the ternary catalyst from the literature. The differential adsorption energy (Q_{diff}) with CO_2 uptake from the microcalorimetric analysis of CO_2 loading on the reduced catalyst is shown in Figure 3. The CO_2 uptake at sites of different strength on the fresh and reduced catalysts are reported in Table S2. Q_{diff} values higher than 150 kJ/mol on the reduced catalyst indicated the presence of strong basic sites which were absent in the fresh catalyst.

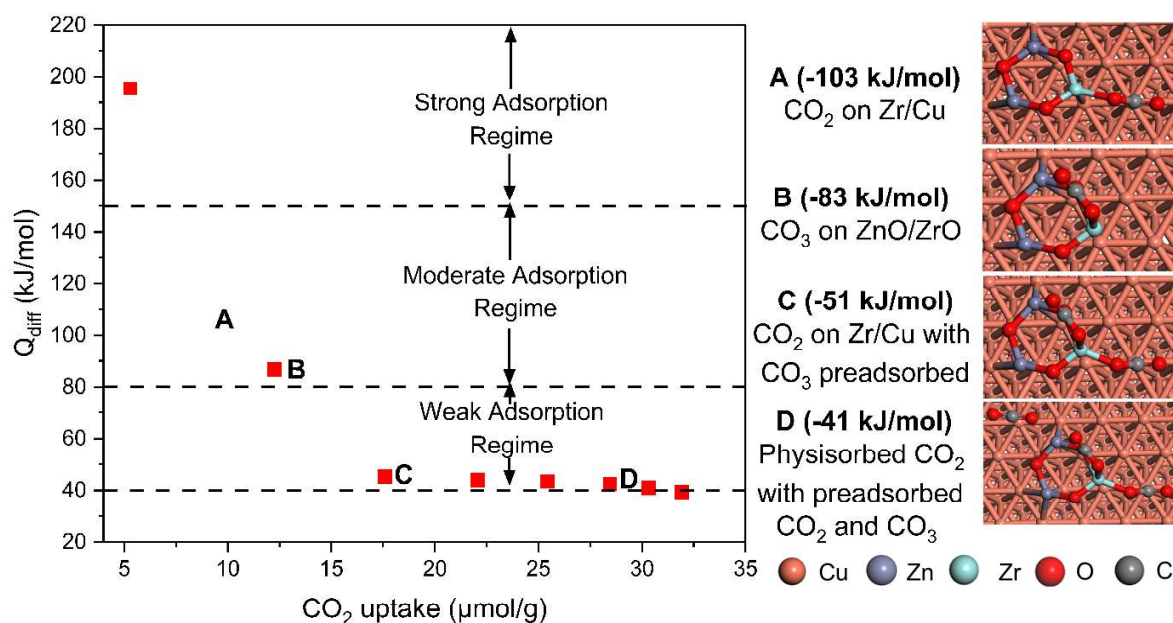


Figure 3-Differential adsorption energy (Q_{diff}) of CO_2 on reduced $Cu_2Zn_1Al_{0.7}Zr_{0.3}$ catalyst against CO_2 loading, obtained from microcalorimetric analysis. Corresponding schematic of CO_2 adsorption on the $Zr_1Zn_2O_3/Cu(111)$ DFT catalyst model showing adsorption at different active sites and their adsorption strength are also shown.

Systematic analysis of the adsorption energy of a single and multiple CO_2 molecules computed using DFT simulations at various interfacial sites on the $Zr_1Zn_2O_3/Cu(111)$ catalyst revealed a bidentate CO_2 at the Zr/Cu interface, as indicated by A in Figure 3 to be the most favorable for single molecular adsorption. Wang et al. [35] confirmed the formation of CO_3^{2-} due to CO_2 adsorption on a Cu/ZnO/ZrO₂ catalyst from analysis of the in-situ DRIFT spectra. The adsorption energy of CO_3^{2-} species on ZnO_x/ZrO_x interface of the $Zr_1Zn_2O_3/Cu(111)$ catalyst, as indicated by B in Figure 3 was computed to be -83 kJ/mol which was in excellent agreement with the adsorption energy from the microcalorimetry analysis during CO_2 loading. With systematic increase in the number of CO_2 molecules adsorbed on the $Zr_1Zn_2O_3/Cu(111)$ catalyst, as indicated by C and D in Figure 3 (2 and 3 CO_2 molecules respectively), the DFT computed differential adsorption energy were again in excellent agreement with the microcalorimetric analysis. These results indicate that the active site features in our model $Zr_1Zn_2O_3/Cu(111)$ catalyst and the adsorption configurations of CO_2 sampled on these sites are representative of operando CO_2 adsorption on the ternary catalyst.

As an additional confirmation of the representativeness of the catalyst model, DFT computed IR frequencies of the HCOO, CH₃O and CH₃OH species which are commonly reported intermediates during CO_2 reduction on ternary Cu/ZnO/ZrO₂ catalyst [35], adsorbed at the Zr/Cu and the Zn/Cu

1
2
3
4 interfaces of the $Zr_1Zn_2O_3/Cu(111)$ catalyst were compared with the frequencies of the same
5 species reported from operando DRIFTS analysis in the literature (Section S4.1 and Table S1).
6 Good agreement between the computed and experimental frequencies of the probe species further
7 indicates the catalyst model to have representative features of the actual catalyst.
8
9

10 **3.3 Mechanism and reaction pathway analysis on the $Zr_1Zn_2O_3/Cu(111)$ catalyst**

11 DFT simulations of CO_2 adsorption on the $Zr_1Zn_2O_3/Cu(111)$ catalyst showed strong
12 chemisorption of CO_2 at the Zr/Cu interface (-103 kJ/mol) and weaker chemisorption at the Zn/Cu
13 interface (-16.4 kJ/mol). Despite the huge difference in the adsorption energy of CO_2 on these two
14 interfacial sites, both the Zr/Cu and Zn/Cu interfaces were considered as the active sites for CO_2
15 hydrogenation to elucidate the role of individual components of the ternary Cu/ZnO/ ZrO_2 catalyst.
16 The dissociative adsorption of H_2 on Cu(111) sites was found to be facile, with hydrogen atoms
17 occupying the hollow sites on Cu(111) surface with an adsorption energy of -38.9 kJ/mol.
18 Continuous availability of the H atom near the vicinity of the Zr/Cu and Zn/Cu interfaces, where
19 the carbonaceous species were adsorbed was assumed for the mechanistic investigation. The DFT
20 computed reaction pathways and energy profiles on the Zr/Cu and Zn/Cu interfaces are discussed
21 in detail in sections 3.3.1 and 3.3.2 respectively. Based on the reaction network and the DFT
22 computed thermodynamic and kinetic parameters, a detailed kinetic model was developed and
23 validated against the catalytic performance data (Section 3.3.3). The validated kinetic model was
24 used to analyze the reaction pathways and reaction rates at different zones of the catalyst bed
25 (Section 3.3.4).
26
27
28
29
30
31
32
33

34 **3.3.1 The mechanism on the Zr/Cu interface**

35 The free energy profile for CO_2 hydrogenation to methanol on the Zr/Cu interface of the
36 $Zr_1Zn_2O_3/Cu(111)$ model that takes place through the formate and the carboxyl pathways are
37 shown in Figure 4a. The geometries of reaction intermediates, transition states of elementary
38 reactions and the potential energy profiles for the Zr/Cu interface are provided in Figures S3, S4,
39 and S7 respectively. CO_2 hydrogenation initiated with the adsorption of CO_2^* ($\Delta G_{ads} = -0.36$ eV)
40 on the interface of Zr and Cu with O and C atoms bonded to Zr and Cu atoms, respectively (Figure
41 S3(a)). H_2 adsorbed dissociatively on the hollow sites of Cu as $2H^*$ ($\Delta G_{ads} = 0.32$ eV). CO_2^*
42 underwent hydrogenation to form either $HCOO^*$ or $COOH^*$ as the first intermediate species
43 leading to the formate and the carboxyl pathways respectively. $HCOO^*$ was bound in a bidentate
44 configuration with the O atoms on Zr and Cu, as shown in SI (Figure S3(b)). Alternatively, the
45 free O atom of CO_2^* was hydrogenated to form $COOH^*$ as a bidentate species (Figure S3(h)).
46 Between the two steps, $HCOO^*$ formation was more exergonic ($\Delta G_{rxn} = -0.77$ eV) than the $COOH^*$
47 formation ($\Delta G_{rxn} = -0.06$ eV). The activation free energy barriers calculated for the two steps
48
49
50
51
52
53
54
55
56
57
58
59
60
61
62
63
64
65

showed that the formation of HCOO^* ($\Delta G^\ddagger = 0.25$ eV) is kinetically more favorable than COOH^* ($\Delta G^\ddagger = 0.69$ eV).

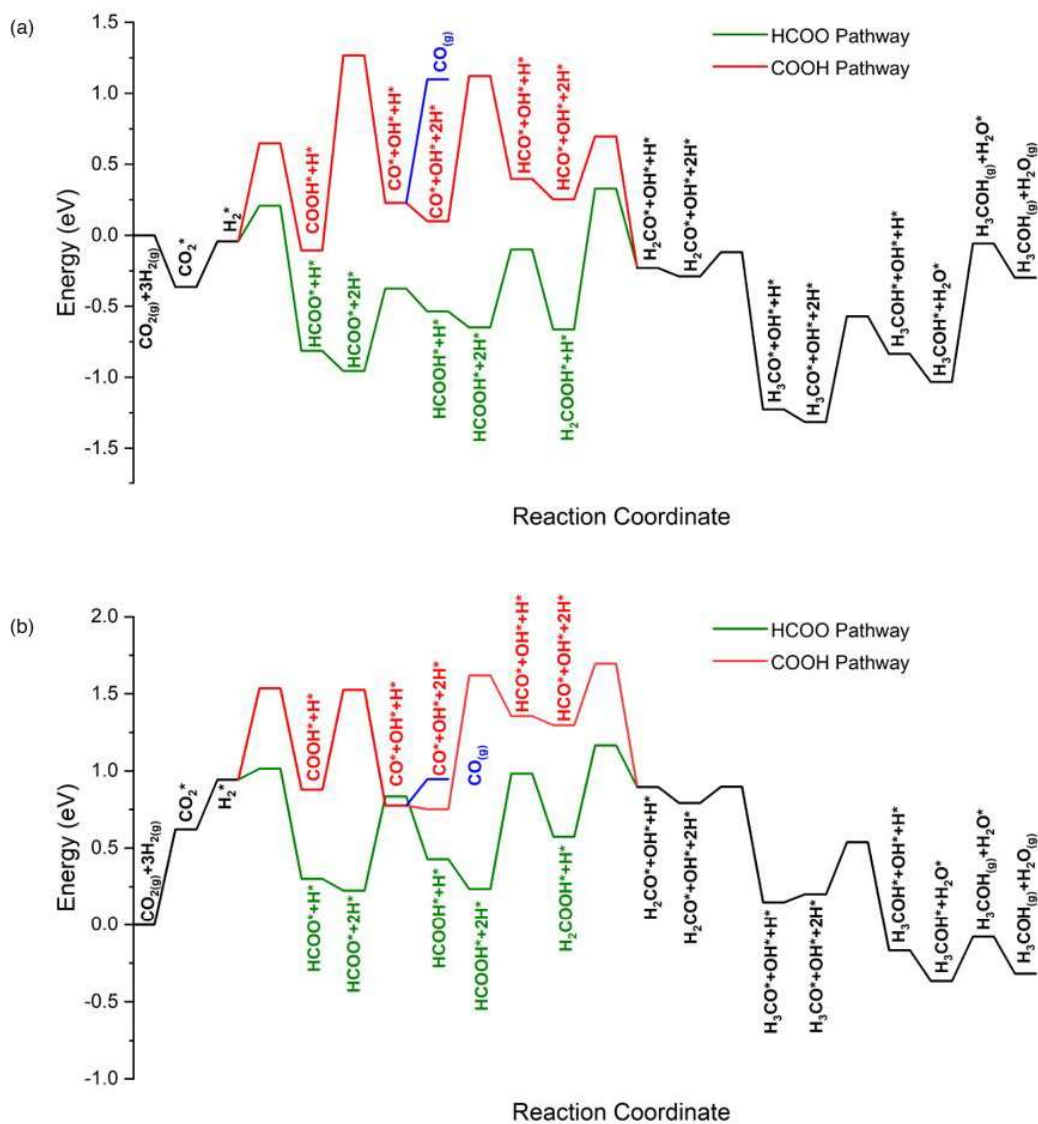


Figure 4-Free energy profile showing different pathways for CO_2 hydrogenation to methanol on the (a) Zr/Cu interface and (b) Zn/Cu interface of the $\text{Zr}_1\text{Zn}_2\text{O}_3/\text{Cu}$ (111) catalyst model. Green – HCOO pathway; Red – COOH pathway; Black – Common intermediates on both HCOO and COOH pathways; Blue – CO desorption in COOH pathway

HCOO^* underwent hydrogenation on the oxygen to form HCOOH^* ($\Delta G_{\text{rxn}} = 0.42$ eV, $\Delta G^\ddagger = 0.58$ eV) species. The formed HCOOH^* species underwent further hydrogenation to H_2COOH^* ($\Delta G_{\text{rxn}} = -0.01$ eV, $\Delta G^\ddagger = 0.55$ eV), which was highly favorable compared to its dissociation $\text{HCO}^* + \text{OH}^*$ ($\Delta G_{\text{rxn}} = 0.8$ eV). H_2COOH^* species dissociated to $\text{H}_2\text{CO}^* + \text{OH}^*$ and was endergonic ($\Delta G_{\text{rxn}} = 0.44$ eV, $\Delta G^\ddagger = 0.99$ eV). This was followed by further hydrogenation to form H_3CO^* ($\Delta G_{\text{rxn}} = -0.94$ eV, $\Delta G^\ddagger = 0.17$ eV) species. H_3CO^* finally hydrogenated to H_3COH^* ($\Delta G_{\text{rxn}} = 0.48$ eV, $\Delta G^\ddagger = 0.74$ eV)

1
2
3
4 and the remaining OH* on Cu(111) got hydrogenated to H₂O* ($\Delta G_{\text{rxn}} = -0.2$ eV). H₃COH* and
5 H₂O* finally desorbed with $\Delta G_{\text{des}} = 0.97$ eV and $\Delta G_{\text{des}} = -0.24$ eV, respectively.
6

7
8 On the COOH pathway, the first intermediate COOH* dissociated to form CO* and OH* with a
9 high activation free energy barrier of ($\Delta G^\ddagger = 1.37$ eV). The CO* species formed and interacted
10 with the Zr/Cu interface while the OH* species moved on to the Cu hollow site. CO* hydrogenated
11 to HCO* ($\Delta G_{\text{rxn}} = 0.30$ eV, $\Delta G^\ddagger = 1.02$ eV) followed by its further hydrogenation to form H₂CO*
12 ($\Delta G_{\text{rxn}} = -0.48$ eV, $\Delta G^\ddagger = 0.44$ eV). H₂CO* species was the common intermediate observed for both
13 the HCOO and COOH pathways, forming H₃COH*.
14
15

16 17 **3.3.2 The mechanism on the Zn/Cu interface**

18 The free energy profile for CO₂ hydrogenation to methanol on the Zn/Cu interface of the
19 Zr₁Zn₂O₃/Cu(111) catalyst model is shown in Figure 4b. The geometries of the reaction
20 intermediates, transition states of elementary reactions and the potential energy profiles for the
21 Zr/Cu interface are provided in Figures S5, S6, and S8 respectively. The mechanism initiated with
22 CO₂ adsorption on the interface of Zn and Cu with an adsorption free energy of ($\Delta G_{\text{ads}} = 0.62$ eV).
23 H₂ adsorbed dissociatively with an adsorption free energy of ($\Delta G_{\text{ads}} = 0.32$ eV). The formation of
24 HCOO* ($\Delta G_{\text{rxn}} = -0.64$ eV, $\Delta G^\ddagger = 0.07$ eV) was highly exergonic compared to formation of COOH*
25 ($\Delta G_{\text{rxn}} = -0.06$ eV, $\Delta G^\ddagger = 0.59$ eV). HCOO* hydrogenated to HCOOH* ($\Delta G_{\text{rxn}} = 0.20$ eV, $\Delta G^\ddagger = 0.61$
26 eV), which was less favorable than on the Zr/Cu interface. Unlike the exergonic HCOOH*
27 hydrogenation to H₂COOH* on the Zr/Cu interface, it was endergonic ($\Delta G_{\text{rxn}} = 0.33$ eV, $\Delta G^\ddagger = 0.75$
28 eV) on the Zn/Cu interface. The H₂COOH* species dissociated to H₂CO* and OH* ($\Delta G_{\text{rxn}} = 0.32$
29 eV, $\Delta G^\ddagger = 0.59$ eV) species, where the latter adsorbed at the hollow site of Cu. H₂CO* further easily
30 hydrogenated to H₃CO* ($\Delta G_{\text{rxn}} = -0.64$ eV, $\Delta G^\ddagger = 0.11$ eV). Finally, H₃CO* and the remaining OH*
31 species on the Cu surface underwent hydrogenation to H₃COH* ($\Delta G_{\text{rxn}} = -0.37$ eV, $\Delta G^\ddagger = 0.34$ eV)
32 and H₂O* ($\Delta G_{\text{rxn}} = -0.2$ eV), respectively. The desorption free energy of H₃COH* on the Zr/Cu
33 interface was 0.97 eV, while it is significantly lower at 0.29 eV on the Zn/Cu interface.
34
35
36
37
38
39
40

41 COOH* dissociated to CO* and OH* ($\Delta G_{\text{rxn}} = -0.10$ eV, $\Delta G^\ddagger = 0.65$ eV), where the former
42 sequentially hydrogenated to form methanol. The desorption of CO* ($\Delta G_{\text{des}} = 0.17$ eV) takes place
43 in parallel to its hydrogenation to HCO* ($\Delta G_{\text{rxn}} = 0.61$ eV, $\Delta G^\ddagger = 0.87$ eV). HCO* can be
44 hydrogenated to H₂CO* ($\Delta G_{\text{rxn}} = -0.40$ eV, $\Delta G^\ddagger = 0.40$ eV), the common intermediate observed for
45 HCOO and COOH routes. The activation free energy barriers of the elementary steps in COOH
46 pathway on the Zn/Cu interface was significantly lower than on the Zr/Cu interface.
47
48
49
50
51
52
53
54
55
56
57
58
59
60
61
62
63
64
65

3.3.3 Microkinetic model: Validation and Species-profiles

All the reactions considered for the microkinetic model are listed in Table S4 together with the forward and backward activation energy barriers and the corresponding pre-exponential factors. The developed microkinetic model coupled with the PFR model was validated against the fixed-bed reactor experimental data and the results are shown in Figures 5 and 6. The activity of the catalyst for CO₂ reduction to methanol was investigated in the packed-bed reactor for a range of temperatures (200-250° C), gas-hourly space velocities (4,500-13,000 h⁻¹) and inlet H₂/CO₂ ratios (See section S.7 of SI). CO₂ conversion increases with temperature and the trend was correctly captured by the microkinetic model. Figure 5a shows the temperature dependence of overall CO₂ conversion and reactor exit CO₂ molar flowrates. Methanol synthesis from CO₂ is an exothermic reaction and reverse water-gas shift reaction, which is endothermic, takes place as a side reaction. At lower temperatures, methanol formation rates are relatively higher than CO as seen in Figure 5b, however, the overall CO₂ conversion is low. The maximum temperature considered was limited to 250° C because a further increase in temperature would shift the thermodynamic equilibrium away from the production of methanol towards CO.

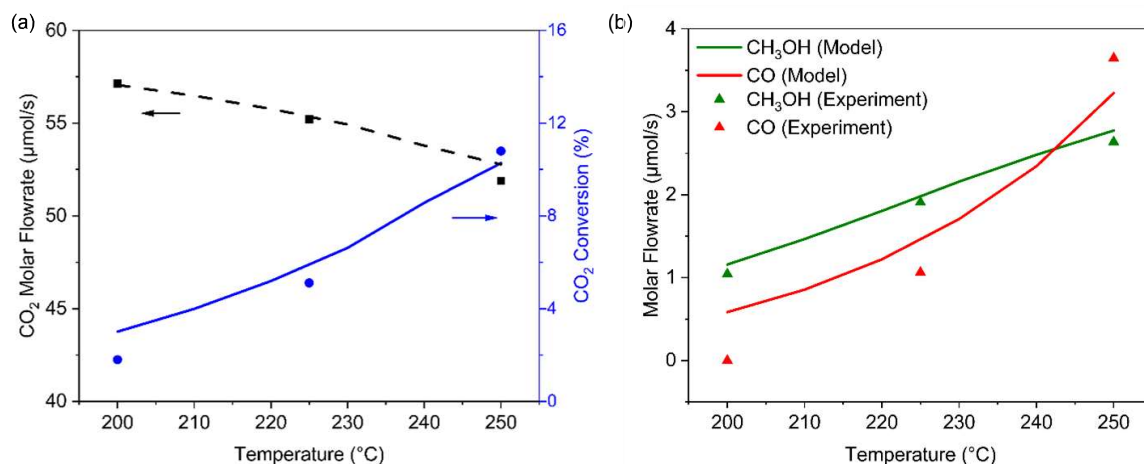


Figure 5- CO₂ conversion and reactor outlet molar flowrates as a function of temperature. All these experiments/model data are measured/computed at P=30 bar. T=250 °C, GHSV=7,000 h⁻¹, inlet p_{H₂}, p_{CO₂}, p_{N₂}=19.9, 6.7, 2.9 (bar) respectively, whenever it is not varied. Symbols represent experimental data points. Lines represent model predicted data points. Color codes: Blue-CO₂ conversion; Black, Green, Red- reactor outlet CO₂, CH₃OH, CO molar flow rates.

Figures 6a and 6b show the dependence of CO₂ conversion (shown in blue symbols) and outlet molar flowrates (shown in dashed columns) on GHSV and the inlet feed composition, respectively. The corresponding model predictions are depicted using lines and solid filled columns. Whenever the reaction parameters were not varied, they were maintained at T=250 °C, GHSV=7,000 h⁻¹, and p_{H₂}, p_{CO₂}, p_{N₂}=19.9, 6.7, 2.9 (bar) respectively. Due to increased residence time, conversion is higher at lower GHSV as seen in Figure 6a. However, methanol production is higher at higher GHSV as more mass of CO₂ flows into the reactor. It is evident from Figure 6b that higher inlet hydrogen partial pressures give higher CO₂ conversions. From Figures 5 and 6, it is evident that

the microkinetic model captured the experimental features reasonably well. The validated kinetic model is then used for further analysis.

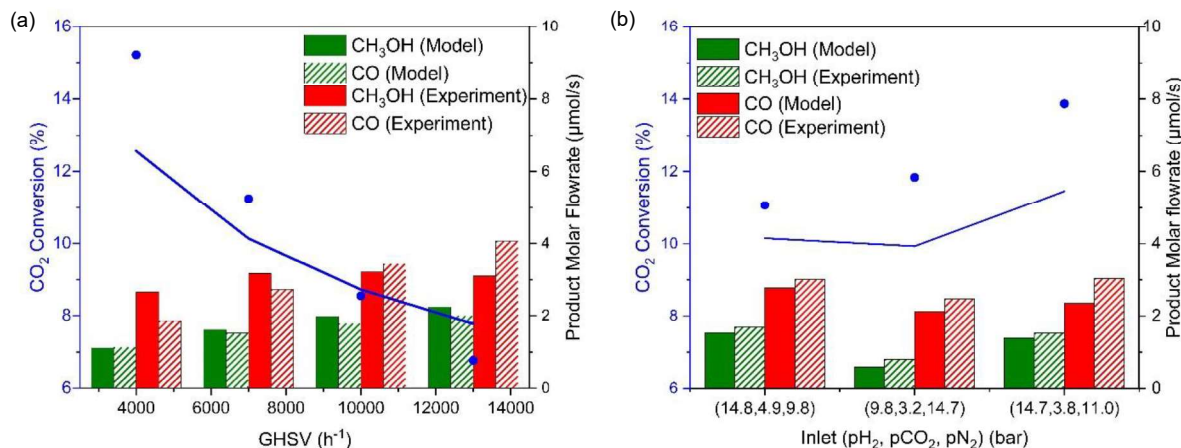


Figure 6- CO₂ conversion, reactor outlet molar flowrates as a function of (a) GHSV and (b) feed ratios. All these experiments/model data are measured/computed at P=30 bar. T=250 °C, GHSV=7000 h⁻¹, inlet pH₂, pCO₂, pN₂=19.9, 6.7, 2.9 (bar) respectively, whenever it is not varied. Symbols and dashed columns represent experimental data points. Lines and solid filled columns represent model predicted data points. Color codes: Blue-CO₂ conversion; Green, Red- reactor outlet CH₃OH, CO molar flow rates

The molar flow rates of unreacted gases and products along the length of the catalyst bed as predicted by the microkinetic model at T=250 °C, GHSV= 7,000 h⁻¹, inlet partial pressure, pH₂= 19.9 bar, pCO₂= 6.7 bar, pN₂= 2.9 bar is shown in Figure 7a, while the corresponding surface coverage of the reaction intermediates is shown in Figure 7b. As expected, there is an increase in the gas-phase concentrations of CH₃OH, CO and H₂O (scale on the right-side axis of Figure 7a) and a decrease in the gas-phase concentrations of CO₂ and H₂ (scale on the left-side axis of Figure 7a) as they get consumed in the reaction. The rate of formation of methanol in the gas phase is higher near the entry of the reactor and it is in line with the behavior of surface species (Figure 7b).

With Cu, Zr/Cu interface, Zn/Cu interface considered as active sites in the microkinetic model, the fractional site coverage of the corresponding most abundant reactive intermediates along the length of the catalyst bed are marked using different line styles: solid for Cu, dashed for Zr/Cu interface and dash-dot for Zn/Cu interface in Figure 7b. Although H# was found to be the key adsorbed species on the Cu site, more than 80% of the Cu sites remained vacant ($\theta_{\#} > 0.8$). Carbonaceous species were found only on the Zr/Cu or Zn/Cu interfaces. Formate (HCOO*) and methoxy (CH₃O*) were the abundant surface species on the Zr/Cu interface, whereas formate (HCOO*) and methanol (CH₃OH*) dominated the Zn/Cu interface. It is worth noting that the rate of disappearance of formate and the rate of appearance of methoxy (on Zr/Cu) and methanol (on Zn/Cu) is very high in the initial part of the bed and is explained by the reaction pathway analysis in section 3.3.4. This also corroborates with the behavior of gas phase species where the formation of methanol is high near the entrance of the reactor. The microkinetic model predicted surface

intermediates have been identified as surface species on ternary Cu/ZnO/ZrO₂ catalysts during in-situ DRIFTS analysis of CO₂ hydrogenation under similar reaction conditions in the literature [35,56], validating the computational predictions. Other surface intermediates predicted with lower coverages than these intermediates are shown in Figure S9.

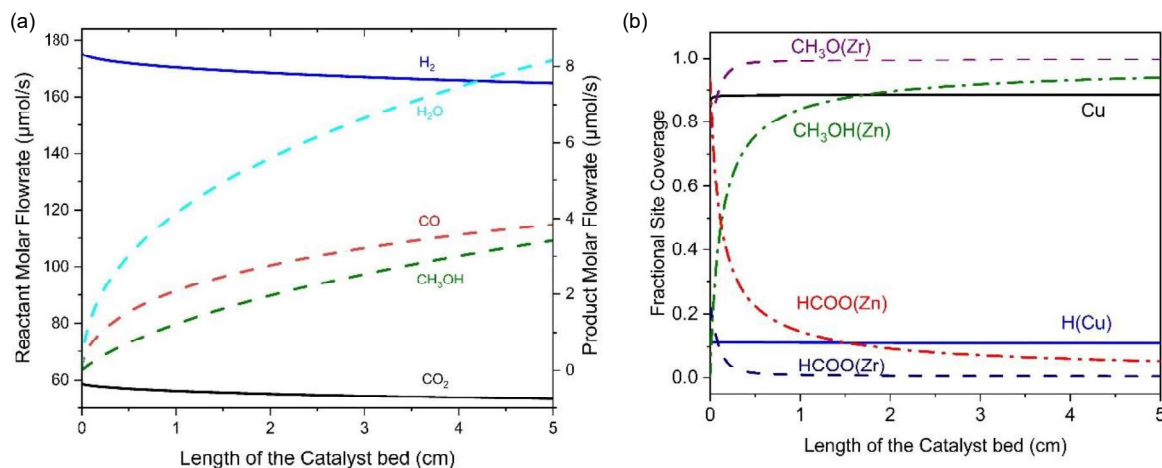


Figure 7-(a)- The gas phase and (b) catalyst surface species as a function of catalyst bed length. In the gas-phase profile, CO₂ and H₂ have their scale on the left and the remaining species have their scale on the right. In the surface species plot, solid lines represent the species on Cu, dashed lines represent the species on Zr/Cu interface and the dot-dashed lines represent the species on Zn/Cu interface. Reaction Conditions: $T=250\text{ }^{\circ}\text{C}$, $P=30\text{ bar}$, $\text{GHSV}=7,000\text{ h}^{-1}$

3.3.4 Reaction pathway analysis

As discussed in section 3.3.1 and 3.3.2, the reaction can either proceed through the formate (right arm of Figure 1) or the carboxyl (left arm of Figure 1) pathways on either Zr/Cu or the Zn/Cu interfaces. The reaction pathway analysis is an outcome of our microkinetic studies and will be useful to understand the reaction behavior and hence better design the catalyst and the reactor system. The reaction pathway analysis was conducted at reaction conditions $T=250\text{ }^{\circ}\text{C}$, $\text{GHSV}=7,000\text{ h}^{-1}$, inlet partial pressure, $p_{\text{H}_2}=19.9\text{ bar}$, $p_{\text{CO}_2}=6.7\text{ bar}$, $p_{\text{N}_2}=2.9\text{ bar}$. The catalyst bed, which effectively is the reactor, is split into four zones and the reaction pathway analysis is individually performed at all these zones: the first 0.05 cm of the reactor is attributed as zone-1; subsequent reaction pathway analyses are conducted at zone-2 (0.05-1.62 cm), zone-3 (1.63-3.31 cm) and zone-4 (3.31-5 cm) of the reactor. The reaction rate for all the elementary reactions in the complete reaction network was calculated at appropriate locations in each of the catalyst zones. Rates of selected elementary reaction steps are collected and presented in Figure 8.

Although the DFT calculated adsorption energy of CO₂ on the Zn/Cu interface was lower than that of the Zr/Cu interface, Figure 8a shows that the rate of CO₂ adsorption was over nine orders of magnitude higher on the Zn/Cu interface. A similar trend was observed in the rate of methanol formation, which was also higher by a similar magnitude, as the CO₂ reduction reactions primarily proceeded through the Zn/Cu interface. This was due to the lower activation barriers of CO₂ hydrogenation steps on the Zn/Cu interface as discussed in section 3.3.2. To further corroborate

1
2
3
4 this, computational CO₂ adsorption/desorption studies on the catalyst bed maintained in the
5 temperature range of 300K-1000K (Section S.8.4 of the SI) were performed, which showed that
6 at the typical methanol synthesis conditions, CO₂ poisoned the Zr sites and only the CO₂ on Zn
7 desorbed (Figure S10). Finally, the microkinetic model with only Zr/Cu interface and Cu sites as
8 the active sites present on the catalyst was simulated, unlike our original microkinetic analysis
9 which included Zr/Cu and Zn/Cu interfaces with Cu sites: The variation of CO₂ conversion with
10 temperatures, GHSV and inlet gas compositions, predicted by this two site microkinetic model are
11 presented in Figure S11. The negligible CO₂ conversion predicted by the model confirmed that the
12 Zr/Cu interface was inactive and CO₂ reduction primarily proceeded along the Zn/Cu interface.
13
14
15
16
17

18 Since the CO₂ reduction rates on the Zn/Cu interface are orders of magnitude higher than that on
19 the Zr/Cu interface, further reaction pathway analysis is presented only for the Zn/Cu interface.
20 The adsorbed CO₂ on the Zn/Cu interface can either hydrogenate to form HCOO* or COOH*
21 species and the DFT calculations showed lower activation free energy barriers for the formation
22 of HCOO*. The rates of these hydrogenation reactions at different zones of the catalyst bed plotted
23 in Figure 8b showed the rate of formation of HCOO* is higher than the rate of formation of
24 COOH* in Zone-1; however, the rates of HCOO* formation decline to zero (Figure 8b) in the
25 downstream zones. This provided a clear explanation of the behavior in Figure 7b, where the
26 fractional coverage of HCOO* species dropped to around 0.2 and that of CH₃OH* species
27 increased to around 0.8 within Zone-1 of the catalyst bed. This clearly indicated that the methanol
28 synthesis primarily takes place through the formate pathway near the reactor entrance, where the
29 rate of methanol formation is also higher (Figure 7a), while the carboxyl pathway is responsible
30 for the production of methanol and CO in the downstream reactor zones.
31
32
33
34
35
36

37 The COOH* species dissociated on the surface to form CO*, which can either desorb (CO
38 formation via RWGS) or further hydrogenate to form methanol through the direct CO
39 hydrogenation pathway via HCO* intermediate. The rates of formation of CO gas and the
40 formation of HCO* by CO hydrogenation, plotted in Figure 8c showed that CO desorption is the
41 likely reaction in Zone-1. The rate of CO desorption gradually decreased along the length of the
42 catalyst bed, while the rate of hydrogenation remained nearly invariant. The higher rate of CO
43 desorption near the inlet of the reactor is also reflected in the higher molar flowrate of CO in the
44 initial catalyst zone (Figure 7a) and the gradually flattening along the catalyst length. Based on the
45 preferential hydrogenation of CO* to form HCO* in the subsequent reactor zones, one can infer
46 that both CO₂ and CO hydrogenation are both important “global” steps for methanol synthesis.
47
48
49
50
51

52 Since CH₂O* is a common intermediate for both the formate and the carboxyl pathway (see Figure
53 1), the rate of formation of CH₂O* in each of these pathways is another quantitative metric to
54 ascertain the pathway towards methanol formation. Figure 8d presents the rate of formation of
55 CH₂O* from H₂COOH* (formate pathway) and from HCO* (carboxyl pathway). Also shown in
56 the figure is the rate of methanol desorption which almost mimics the trend in the rate of formation
57 of CH₂O* from HCO*, and the contribution of the carboxyl pathway to methanol formation (right
58 axis). Figure 8d confirms the inferences in the previous discussions, where the formate pathway
59
60
61
62
63
64
65

contributes towards methanol production in the initial zone of the reactor while the carboxyl pathway almost exclusively contributes towards methanol formation in the later zones. Furthermore, methanol desorption rates corroborate with the gas-phase concentration profile of methanol, where the initial slope is higher, and it gets flatter in the later parts of the reactor.

In summary, the Zn/Cu interface is identified as the active site responsible for methanol synthesis and the reaction route switches from the formate to the carboxyl pathway along the length of the catalyst bed.

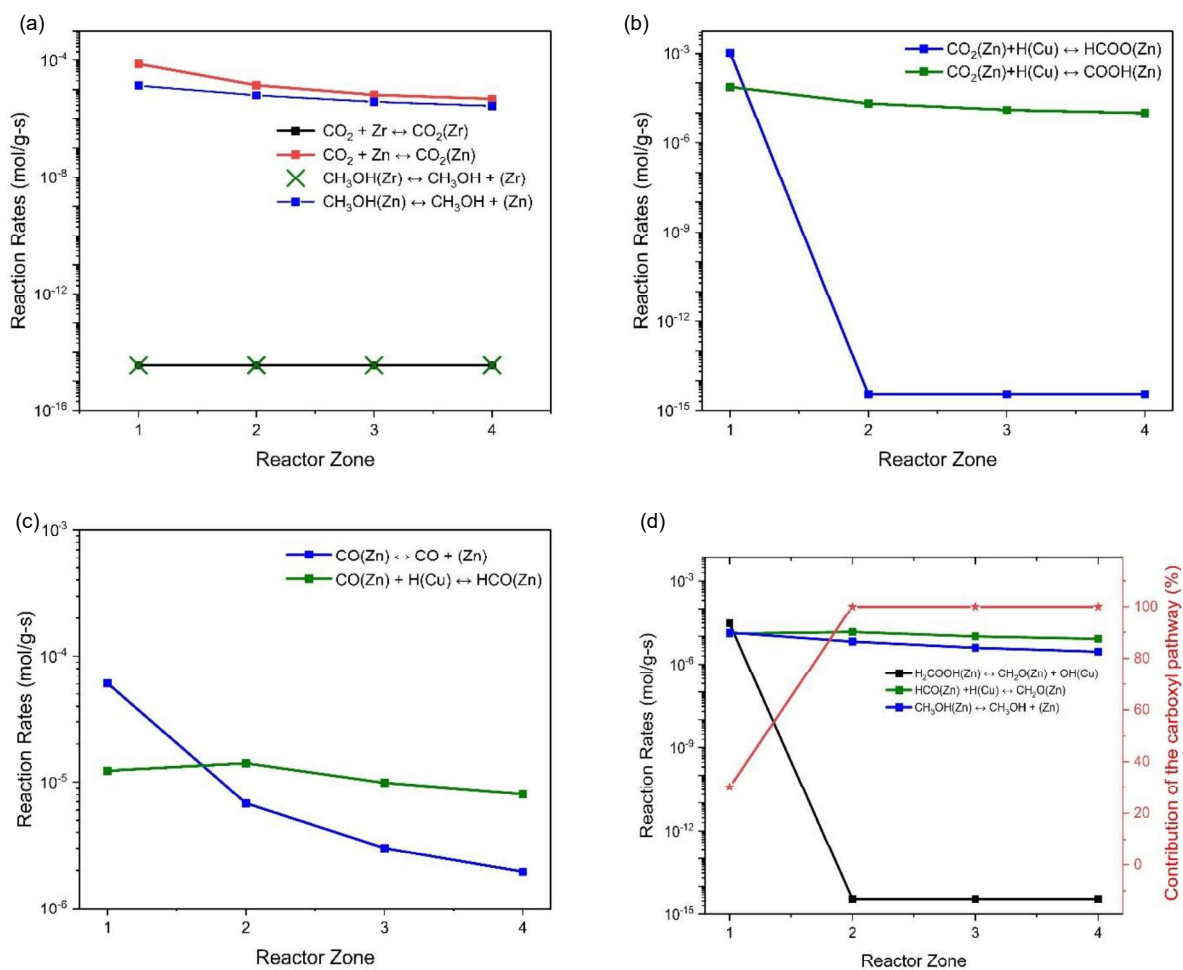


Figure 8- (a) Comparison of CO_2 adsorption rates on Zr/Cu interface and Zn/Cu interface (b) Comparison of CO_2 hydrogenation rates on the Zn-Cu interface to produce HCOO^* and COOH^* (c) Comparison of CO desorption and hydrogenation rates on the Zn-Cu interface (d) Comparison of the contribution of the formate and carboxyl pathway towards methanol synthesis on the Zn-Cu interface. Reaction Conditions: $T=250\text{ }^\circ\text{C}$, $P=30\text{ bar}$, $GHSV=7,000\text{ h}^{-1}$

4 Conclusions

A combination of reactor experiments, detailed DFT simulations of a complex reaction network and a multi-site first-principles microkinetic model were used to understand the mechanistic behavior of the methanol synthesis reaction and to elucidate the role of individual components of the $\text{Cu}_2\text{Zn}_1\text{Al}_{0.7}\text{Zr}_{0.3}$ catalyst.

The $\text{Cu}_2\text{Zn}_1\text{Al}_{0.7}\text{Zr}_{0.3}$ catalyst was synthesized by the coprecipitation method and characterized for the structural features using XRD and TPR techniques. The XRD analysis of the reduced catalyst showed the reduction of CuO to a metallic Cu, with weakly crystalline ZnO and finely dispersed ZrO_2 , indicative of strong interaction between all the catalyst components. The catalytic performance of the ternary catalyst was evaluated in a fixed bed reactor at varying conditions of reaction temperature, reactor pressure, inlet flowrate and composition of the gases.

A computationally tractable catalyst model representative of the inverse catalyst, with active site features validated against microcalorimetric measurements of CO_2 uptake and in-situ DRIFTS analysis of CO_2 hydrogenation was used for detailed mechanistic analysis using DFT simulations. The Zr/Cu interface on the ternary catalyst was identified as the strong CO_2 adsorption site while metallic copper served as the active hydrogen supply site.

A mean-field multi-site reactor-scale microkinetic model based on DFT calculations on the ternary $\text{Cu}_2\text{Zn}_1\text{Al}_{0.7}\text{Zr}_{0.3}$ catalyst was developed and found to predict the catalytic performance and product flow rate well. Despite the Zr/Cu interface being a strong adsorption site for CO_2 , the microkinetic results showed that the Zn/Cu interface is the crucial reaction center at the desired reaction conditions (T-200 to 250°C, P-30 bar). The reaction progressed many orders of magnitude faster on the Zn/Cu interface due to the relatively “moderate” CO_2 binding energy and comparatively lower activation energy barriers for surface reactions than at the Zr/Cu interface. Hence, it is hypothesized that the promotional effect of Zr in the ternary catalyst is probably indirect and not mechanistic. Although the mechanistic investigations by DFT simulations on $\text{Zr}_1\text{Zn}_2\text{O}_3/\text{Cu}(111)$ catalyst indicated that the formate pathway was kinetically dominant, the reaction pathway analyses predicted methanol formation via both the formate and the carboxyl pathways to be relevant. The formate pathway was prevalent in the initial part of the reactor while the carboxyl pathway was dominant in the later part. HCOO^* and CH_3OH^* were found to be the most abundant reaction intermediates on the Zn/Cu interface during the reaction.

Unique insights into the reaction behavior at different parts of the reactor were unraveled due to the multi-site reaction network considerations in the modeling framework, without a priori elimination of reaction pathways. Multistage validations of the computational catalyst model and reaction mechanisms, and thermodynamic consistency analysis enabled development of a first principles detailed kinetic model for the ternary catalyst capable of predicting catalytic performance and product profiles at desired conditions. Microkinetic analysis provides insights

1
2
3
4 into catalyst structure-activity correlations which can effectively be used in rational design of
5 advanced catalytic materials. Insights into the reaction behavior along the reactor enables
6 identification of strategies for optimization and design of appropriate reactors.
7
8
9

10 **CRedit authorship contribution statement**

11 **Balaji C Dharmalingam:** Computational catalyst modeling, computation and analysis of energetics,
12 writing. **Ajay Koushik V:** Development, validation, and analysis of microkinetic model, writing. **Mauro**
13 **Mureddu:** Packed-bed reactor experiments, writing. **Luciano Atzori:** Synthesis and Characterization of
14 the catalyst. **Sarah Lai:** Characterization analysis, writing. **Alberto Pettinau:** Funding acquisition and
15 supervision, **Niket S Kaisare:** Formal analysis, conceptualization, and editing. **Preeti Aghalayam:** Formal
16 analysis, conceptualization, and editing. **Jithin John Varghese:** Formal analysis, conceptualization, and
17 editing.
18
19
20
21
22

23 **Declaration of Competing Interest**

24 The authors declare that they have no known competing financial interests or personal relationships that
25 could have appeared to influence the work reported in this paper.
26
27
28

29 **Acknowledgement**

30 BCD, AKV, NSK, PA and JJV acknowledge the Carbon Capture Utilization and Storage (CCUS)
31 laboratory, IIT Madras for the facilities. The authors acknowledge the use of the High-Performance
32 Computing Environment (HPCE), IIT Madras for the computing resources for the DFT calculations. JJV
33 acknowledges the New Faculty Seed Grant (CHE/19-20/713/NFSC/JITH) from IIT Madras. The
34 experimental part of this study has been performed by SOTACARBO within the Advance Sustainable
35 Technologies for Energy Transition, ASSET project (CUP D43C22002400002), funded by the Regional
36 Government of Sardinia through Sardegna Ricerche.
37
38
39
40
41

42 **Appendix A. Supporting Information**

43 **References**

- 44
45
46
47 [1] J. Blunden, T. Boyer, State of the Climate in 2020, Bull. Am. Meteorol. Soc. 102 (2021)
48 S1–S475. <https://doi.org/10.1175/2021BAMSStateoftheClimate.1>.
49
50 [2] IPCC, Global Warming of 1.5°C: IPCC Special Report on Impacts of Global Warming of
51 1.5°C above Pre-industrial Levels in Context of Strengthening Response to Climate
52 Change, Sustainable Development, and Efforts to Eradicate Poverty, Cambridge
53 University Press, 2022. <https://doi.org/10.1017/9781009157940>.
54
55 [3] T. Sakakura, J.C. Choi, H. Yasuda, Transformation of carbon dioxide, Chem. Rev. 107
56 (2007) 2365–2387. <https://doi.org/10.1021/cr068357u>.
57
58 [4] I. Dimitriou, P. García-Gutiérrez, R.H. Elder, R.M. Cuéllar-Franca, A. Azapagic, R.W.K.
59
60
61
62
63
64
65

- 1
2
3
4 Allen, Carbon dioxide utilisation for production of transport fuels: Process and economic
5 analysis, *Energy Environ. Sci.* 8 (2015) 1775–1789. <https://doi.org/10.1039/c4ee04117h>.
6
- 7
8 [5] K. Li, J.G. Chen, CO₂ Hydrogenation to Methanol over ZrO₂-Containing Catalysts:
9 Insights into ZrO₂ Induced Synergy, *ACS Catal.* 9 (2019) 7840–7861.
10 <https://doi.org/10.1021/acscatal.9b01943>.
11
- 12 [6] F. Zeng, C. Mebrahtu, X. Xi, L. Liao, J. Ren, J. Xie, H.J. Heeres, R. Palkovits, Catalysts
13 design for higher alcohols synthesis by CO₂ hydrogenation: Trends and future
14 perspectives, *Appl. Catal. B Environ.* 291 (2021) 120073.
15 <https://doi.org/10.1016/j.apcatb.2021.120073>.
16
- 17 [7] M. Behrens, F. Studt, I. Kasatkin, S. Kühl, M. Hävecker, F. Abild-Pedersen, S. Zander, F.
18 Girgsdies, P. Kurr, B.-L. Kniep, M. Tovar, R.W. Fischer, J.K. Nørskov, R. Schlögl, The
19 active site of methanol synthesis over Cu/ZnO/Al₂O₃ industrial catalysts., *Science.* 336
20 (2012) 893–897. <https://doi.org/10.1126/science.1219831>.
21
- 22 [8] O. Martin, A.J. Martín, C. Mondelli, S. Mitchell, T.F. Segawa, R. Hauert, C. Drouilly, D.
23 Curulla-Ferré, J. Pérez-Ramírez, Indium oxide as a superior catalyst for methanol
24 synthesis by CO₂ hydrogenation, *Angew. Chemie - Int. Ed.* 55 (2016) 6261–6265.
25 <https://doi.org/10.1002/anie.201600943>.
26
- 27 [9] M. Mureddu, F. Ferrara, A. Pettinau, Highly efficient CuO/ZnO/ZrO₂@SBA-15
28 nanocatalysts for methanol synthesis from the catalytic hydrogenation of CO₂, *Appl.*
29 *Catal. B Environ.* 258 (2019) 117941. <https://doi.org/10.1016/j.apcatb.2019.117941>.
30
- 31 [10] X. Hu, C. Zhao, Q. Guan, X. Hu, W. Li, J. Chen, Selective hydrogenation of CO₂ over a
32 Ce promoted Cu-based catalyst confined by SBA-15, *Inorg. Chem. Front.* 6 (2019) 1799–
33 1812. <https://doi.org/10.1039/c9qi00397e>.
34
- 35 [11] S. Li, L. Guo, T. Ishihara, Hydrogenation of CO₂ to methanol over Cu/AlCeO catalyst,
36 *Catal. Today.* 339 (2020) 352–361. <https://doi.org/10.1016/j.cattod.2019.01.015>.
37
- 38 [12] M. Zabilskiy, K. Ma, A. Beck, J.A. Van Bokhoven, Methanol synthesis over Cu/CeO₂-
39 ZrO₂catalysts: The key role of multiple active components, *Catal. Sci. Technol.* 11 (2021)
40 349–358. <https://doi.org/10.1039/d0cy01762k>.
41
- 42 [13] W. Wang, Z. Qu, L. Song, Q. Fu, CO₂ hydrogenation to methanol over Cu/CeO₂ and
43 Cu/ZrO₂ catalysts: Tuning methanol selectivity via metal-support interaction, *J. Energy*
44 *Chem.* 40 (2020) 22–30. <https://doi.org/10.1016/j.jechem.2019.03.001>.
45
- 46 [14] F. Arena, K. Barbera, G. Italiano, G. Bonura, L. Spadaro, F. Frusteri, Synthesis,
47 characterization and activity pattern of Cu-ZnO/ZrO₂ catalysts in the hydrogenation of
48 carbon dioxide to methanol, *J. Catal.* 249 (2007) 185–194.
49 <https://doi.org/10.1016/j.jcat.2007.04.003>.
50
- 51 [15] T. Witoon, N. Kachaban, W. Donphai, P. Kidkhunthod, K. Faungnawakij, M.
52 Chareonpanich, J. Limtrakul, Tuning of catalytic CO₂ hydrogenation by changing
53 composition of CuO-ZnO-ZrO₂ catalysts, *Energy Convers. Manag.* 118 (2016) 21–31.
54
55
56
57
58
59
60
61
62
63
64
65

1
2
3
4
5
6
7
8
9
10
11
12
13
14
15
16
17
18
19
20
21
22
23
24
25
26
27
28
29
30
31
32
33
34
35
36
37
38
39
40
41
42
43
44
45
46
47
48
49
50
51
52
53
54
55
56
57
58
59
60
61
62
63
64
65

<https://doi.org/10.1016/j.enconman.2016.03.075>.

- [16] G. Bonura, M. Cordaro, C. Cannilla, F. Arena, F. Frusteri, The changing nature of the active site of Cu-Zn-Zr catalysts for the CO₂ hydrogenation reaction to methanol, *Appl. Catal. B Environ.* 152–153 (2014) 152–161. <https://doi.org/10.1016/j.apcatb.2014.01.035>.
- [17] E. Frei, A. Schaadt, T. Ludwig, H. Hillebrecht, I. Krossing, The influence of the precipitation/ageing temperature on a Cu/ZnO/ZrO₂ catalyst for methanol synthesis from H₂ and CO₂, *ChemCatChem.* 6 (2014) 1721–1730. <https://doi.org/10.1002/cctc.201300665>.
- [18] M.Z. Ramli, S.S.A. Syed-Hassan, A. Hadi, Performance of Cu-Zn-Al-Zr catalyst prepared by ultrasonic spray precipitation technique in the synthesis of methanol via CO₂ hydrogenation, *Fuel Process. Technol.* 169 (2018) 191–198. <https://doi.org/10.1016/j.fuproc.2017.10.004>.
- [19] P. Gao, R. Xie, H. Wang, L. Zhong, L. Xia, Z. Zhang, W. Wei, Y. Sun, Cu/Zn/Al/Zr catalysts via phase-pure hydrotalcite-like compounds for methanol synthesis from carbon dioxide, *J. CO₂ Util.* 11 (2015) 41–48. <https://doi.org/10.1016/j.jcou.2014.12.008>.
- [20] Y. Zhang, L. Zhong, H. Wang, P. Gao, X. Li, S. Xiao, G. Ding, W. Wei, Y. Sun, Catalytic performance of spray-dried Cu/ZnO/Al₂O₃/ZrO₂ catalysts for slurry methanol synthesis from CO₂ hydrogenation, *J. CO₂ Util.* 15 (2016) 72–82. <https://doi.org/10.1016/j.jcou.2016.01.005>.
- [21] P. Gao, F. Li, H. Zhan, N. Zhao, F. Xiao, W. Wei, L. Zhong, H. Wang, Y. Sun, Influence of Zr on the performance of Cu/Zn/Al/Zr catalysts via hydrotalcite-like precursors for CO₂ hydrogenation to methanol, *J. Catal.* 298 (2013) 51–60. <https://doi.org/10.1016/j.jcat.2012.10.030>.
- [22] A. Arandia, J. Yim, H. Warraich, E. Leppäkangas, R. Bes, A. Lempelto, L. Gell, H. Jiang, K. Meinander, T. Viinikainen, S. Huotari, K. Honkala, R.L. Puurunen, Effect of atomic layer deposited zinc promoter on the activity of copper-on-zirconia catalysts in the hydrogenation of carbon dioxide to methanol, *Appl. Catal. B Environ.* 321 (2023) 122046. <https://doi.org/10.1016/j.apcatb.2022.122046>.
- [23] L. Gell, A. Lempelto, T. Kiljunen, K. Honkala, Influence of a Cu-zirconia interface structure on CO₂ adsorption and activation, *J. Chem. Phys.* 154 (2021) 214707. <https://doi.org/10.1063/5.0049293>.
- [24] S. Kattel, P. Liu, J.G. Chen, Tuning Selectivity of CO₂ Hydrogenation Reactions at the Metal/Oxide Interface, *J. Am. Chem. Soc.* 139 (2017) 9739–9754. <https://doi.org/10.1021/jacs.7b05362>.
- [25] S. Kattel, B. Yan, Y. Yang, J.G. Chen, P. Liu, Optimizing Binding Energies of Key Intermediates for CO₂ Hydrogenation to Methanol over Oxide-Supported Copper, *J. Am. Chem. Soc.* 138 (2016) 12440–12450. <https://doi.org/10.1021/jacs.6b05791>.
- [26] P. Gao, F. Li, N. Zhao, F. Xiao, W. Wei, L. Zhong, Y. Sun, Influence of modifier (Mn,

- 1
2
3
4 La, Ce, Zr and Y) on the performance of Cu/Zn/Al catalysts via hydrotalcite-like
5 precursors for CO₂ hydrogenation to methanol, *Appl. Catal. A Gen.* 468 (2013) 442–452.
6 <https://doi.org/10.1016/j.apcata.2013.09.026>.
7
8
9 [27] H. Li, L. Wang, X. Gao, F.S. Xiao, Cu/ZnO/Al₂O₃ Catalyst Modulated by Zirconia with
10 Enhanced Performance in CO₂ Hydrogenation to Methanol, *Ind. Eng. Chem. Res.* 61
11 (2022) 10446–10454. <https://doi.org/10.1021/acs.iecr.2c00172>.
12
13 [28] Q.L. Tang, W.T. Zou, R.K. Huang, Q. Wang, X.X. Duan, Effect of the components'
14 interface on the synthesis of methanol over Cu/ZnO from CO₂/H₂: A microkinetic analysis
15 based on DFT + U calculations, *Phys. Chem. Chem. Phys.* 17 (2015) 7317–7333.
16 <https://doi.org/10.1039/c4cp05518g>.
17
18 [29] K. Mondal, Megha, A. Banerjee, A. Fortunelli, M. Walter, M. Moseler, Ab Initio
19 Modeling of the ZnO-Cu(111) Interface, *J. Phys. Chem. C.* 126 (2022) 764–771.
20 <https://doi.org/10.1021/acs.jpcc.1c09170>.
21
22 [30] S. Polierer, J. Jelic, S. Pitter, F. Studt, On the Reactivity of the Cu/ZrO₂ System for the
23 Hydrogenation of CO₂ to Methanol: A Density Functional Theory Study, *J. Phys. Chem.*
24 *C.* 123 (2019) 26904–26911. <https://doi.org/10.1021/acs.jpcc.9b06500>.
25
26 [31] C. Wu, L. Lin, J. Liu, J. Zhang, F. Zhang, T. Zhou, N. Rui, S. Yao, Y. Deng, F. Yang, W.
27 Xu, J. Luo, Y. Zhao, B. Yan, X.D. Wen, J.A. Rodriguez, D. Ma, Inverse ZrO₂/Cu as a
28 highly efficient methanol synthesis catalyst from CO₂ hydrogenation, *Nat. Commun.* 11
29 (2020) 5767. <https://doi.org/10.1038/s41467-020-19634-8>.
30
31 [32] J. Wang, G. Li, Z. Li, C. Tang, Z. Feng, H. An, H. Liu, T. Liu, C. Li, A highly selective
32 and stable ZnO-ZrO₂ solid solution catalyst for CO₂ hydrogenation to methanol, *Sci. Adv.*
33 3 (2017) 1–11. <https://doi.org/10.1126/sciadv.1701290>.
34
35 [33] K. Larmier, W.C. Liao, S. Tada, E. Lam, R. Verel, A. Bansode, A. Urakawa, A. Comas-
36 Vives, C. Copéret, CO₂-to-Methanol Hydrogenation on Zirconia-Supported Copper
37 Nanoparticles: Reaction Intermediates and the Role of the Metal-Support Interface,
38 *Angew. Chemie - Int. Ed.* 56 (2017) 2318–2323. <https://doi.org/10.1002/anie.201610166>.
39
40 [34] S. Kattel, P.J. Ramírez, J.G. Chen, J.A. Rodriguez, P. Liu, Active sites for CO₂
41 hydrogenation to methanol on Cu/ZnO catalysts, *Science.* 355 (2017) 1296–1299.
42 <https://doi.org/10.1126/science.aal3573>.
43
44 [35] Y. Wang, S. Kattel, W. Gao, K. Li, P. Liu, J.G. Chen, H. Wang, Exploring the ternary
45 interactions in Cu–ZnO–ZrO₂ catalysts for efficient CO₂ hydrogenation to methanol, *Nat.*
46 *Commun.* 10 (2019) 1166. <https://doi.org/10.1038/s41467-019-09072-6>.
47
48 [36] H. Chen, H. Cui, Y. Lv, P. Liu, F. Hao, W. Xiong, H. Luo, CO₂ hydrogenation to
49 methanol over Cu/ZnO/ZrO₂ catalysts: Effects of ZnO morphology and oxygen vacancy,
50 *Fuel.* 314 (2022) 123035. <https://doi.org/10.1016/j.fuel.2021.123035>.
51
52 [37] D. Kopač, B. Likozar, M. Huš, Catalysis of material surface defects: Multiscale modeling
53 of methanol synthesis by CO₂ reduction on copper, *Appl. Surf. Sci.* 497 (2019) 143783.
54
55
56
57
58
59
60
61
62
63
64
65

1
2
3
4
5
6
7
8
9
10
11
12
13
14
15
16
17
18
19
20
21
22
23
24
25
26
27
28
29
30
31
32
33
34
35
36
37
38
39
40
41
42
43
44
45
46
47
48
49
50
51
52
53
54
55
56
57
58
59
60
61
62
63
64
65

<https://doi.org/10.1016/j.apsusc.2019.143783>.

- [38] M. Mureddu, S. Lai, L. Atzori, E. Rombi, F. Ferrara, A. Pettinau, M.G. Cutrufello, Ex-ldh-based catalysts for CO₂ conversion to methanol and dimethyl ether, *Catalysts*. 11 (2021) 615. <https://doi.org/10.3390/catal11050615>.
- [39] H.P. Klug, L.E. Alexander, *X-Ray Diffraction Procedures: For Polycrystalline and Amorphous Materials*, 2nd Edition, Wiley-Interscience publications, 1974.
- [40] A. Pettinau, M. Mureddu, F. Ferrara, Carbon Dioxide Conversion into Liquid Fuels by Hydrogenation and Photoelectrochemical Reduction: Project Description and Preliminary Experimental Results, *Energy Procedia*. 114 (2017) 6893–6904. <https://doi.org/10.1016/j.egypro.2017.03.1832>.
- [41] G. Lombardelli, M. Mureddu, S. Lai, F. Ferrara, A. Pettinau, L. Atzori, A. Conversano, M. Gatti, CO₂ hydrogenation to methanol with an innovative Cu/Zn/Al/Zr catalyst: Experimental tests and process modeling, *J. CO₂ Util.* 65 (2022) 102240. <https://doi.org/10.1016/j.jcou.2022.102240>.
- [42] G. Kresse, J. Furthmüller, Efficient iterative schemes for ab initio total-energy calculations using a plane-wave basis set, *Phys. Rev. B - Condens. Matter Mater. Phys.* 54 (1996) 11169–11186. <https://doi.org/10.1103/PhysRevB.54.11169>.
- [43] J.P. Perdew, K. Burke, M. Ernzerhof, Generalized gradient approximation made simple, *Phys. Rev. Lett.* 77 (1996) 3865–3868. <https://doi.org/10.1103/PhysRevLett.77.3865>.
- [44] D. Joubert, From ultrasoft pseudopotentials to the projector augmented-wave method, *Phys. Rev. B - Condens. Matter Mater. Phys.* 59 (1999) 1758–1775. <https://doi.org/10.1103/PhysRevB.59.1758>.
- [45] A. Allouche, Software News and Updates Gabedit — A Graphical User Interface for Computational Chemistry Softwares, *J. Comput. Chem.* 32 (2012) 174–182. <https://doi.org/10.1002/jcc>.
- [46] M.E. Straumanis, L.S. Yu, Lattice parameters, densities, expansion coefficients and perfection of structure of Cu and of Cu–In α phase, *Acta Crystallogr. Sect. A*. 25 (1969) 676–682. <https://doi.org/10.1107/S0567739469001549>.
- [47] H.J. Monkhorst, J.D. Pack, Special points for Brillouin-zone integrations, *Phys. Rev. B*. 13 (1976) 5188–5192. <https://doi.org/10.1103/PhysRevB.13.5188>.
- [48] A. Heyden, A.T. Bell, F.J. Keil, Efficient methods for finding transition states in chemical reactions: Comparison of improved dimer method and partitioned rational function optimization method, *J. Chem. Phys.* 123 (2005) 224101. <https://doi.org/10.1063/1.2104507>.
- [49] M.E. Coltrin, R.J. Kee, F.M. Rupley, Surface chemkin: A general formalism and software for analyzing heterogeneous chemical kinetics at a gas-surface interface, *Int. J. Chem. Kinet.* 23 (1991) 1111–1128. <https://doi.org/10.1002/kin.550231205>.

- 1
2
3
4 [50] L.C. Grabow, M. Mavrikakis, Mechanism of methanol synthesis on cu through CO₂ and
5 CO hydrogenation, ACS Catal. 1 (2011) 365–384. <https://doi.org/10.1021/cs200055d>.
6
7
8 [51] J. Park, J. Cho, Y. Lee, M.J. Park, W.B. Lee, Practical microkinetic modeling approach
9 for methanol synthesis from syngas over a Cu-based catalyst, Ind. Eng. Chem. Res. 58
10 (2019) 8663–8673. <https://doi.org/10.1021/acs.iecr.9b01254>.
11
12 [52] A.K. Raghu, N.S. Kaisare, Microkinetic Modeling and Analysis of CO₂ Methanation on
13 Ruthenium, Ind. Eng. Chem. Res. 59 (2020) 16161–16169.
14 <https://doi.org/10.1021/acs.iecr.0c02685>.
15
16 [53] D. Schmider, L. Maier, O. Deutschmann, Reaction Kinetics of CO and CO₂ Methanation
17 over Nickel, Ind. Eng. Chem. Res. 60 (2021) 5792–5805.
18 <https://doi.org/10.1021/acs.iecr.1c00389>.
19
20 [54] T. Reichenbach, K. Mondal, M. Jäger, T. Vent-Schmidt, D. Himmel, V. Dybbert, A.
21 Bruix, I. Krossing, M. Walter, M. Moseler, Ab initio study of CO₂ hydrogenation
22 mechanisms on inverse ZnO/Cu catalysts, J. Catal. 360 (2018) 168–174.
23 <https://doi.org/10.1016/j.jcat.2018.01.035>.
24
25 [55] T. Lunkenbein, J. Schumann, M. Behrens, R. Schlögl, M.G. Willinger, Formation of a
26 ZnO Overlayer in Industrial Cu/ZnO/Al₂O₃ Catalysts Induced by Strong Metal-Support
27 Interactions, Angew. Chemie - Int. Ed. 54 (2015) 4544–4548.
28 <https://doi.org/10.1002/anie.201411581>.
29
30 [56] F.C.F. Marcos, F.M. Cavalcanti, D.D. Petrolini, L. Lin, L.E. Betancourt, S.D. Senanayake,
31 Effect of operating parameters on H₂/CO₂ conversion to methanol over Cu-Zn oxide
32 supported on ZrO₂ polymorph catalysts : Characterization and kinetics, Chem. Eng. J. 427
33 (2022) 130947. <https://doi.org/10.1016/j.cej.2021.130947>.
34
35
36
37
38
39
40
41
42
43
44
45
46
47
48
49
50
51
52
53
54
55
56
57
58
59
60
61
62
63
64
65